PMM Meeting
Oct 2016
Houston, TX

Orographic Precipitation Processes
- From TRMM to GPM -

Ana P. Barros, Yajuan (Viola) Duan, Malarvizhi Arulraj

Department of Civil and Environmental Engineering, Pratt School of Engineering, Duke University, NC

1. Aerosol-cloud-rainfall Interactions over Complex Terrain

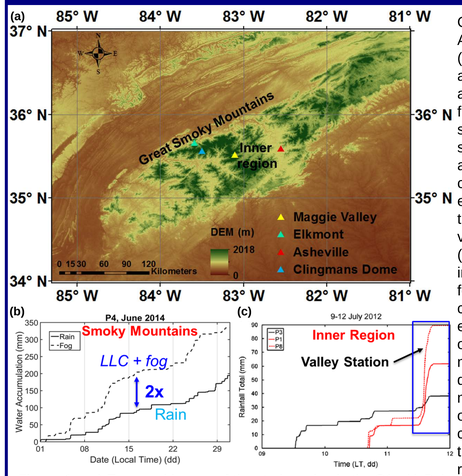

Figure 1 – *a) Topographic map of the study region in the SA ; b) Rain accumulations from co-located fog and rain gauges at a high elevation station (Clingmans Dome, 1956 m MSL) in the GSM during June 2014; c) Cumulative rainfall of a summer event (July 09-12, 2012) in the inner SA region during Intensive Observing Periods (IOPs). Note that two ridges locations (P1 and P3) are indicated by solid lines and the valley site (P8) is indicated by the dashed line (Wilson and Barros, 2015).*

On ridge tops on the western slopes of the Southern Appalachians (SA), in the Great Smoky Mountains (GSM), lateral precipitation that results from fog advection and low-level cloud (LLC) immersion, accounts for a significant fraction of the annual freshwater input, which is especially critical in the warm seasons and in drought years. For example, Figure 1b shows that almost the twice amount of precipitation accumulations are recorded from the fog collector compared to the co-located raingauge at a high elevation station (Clingmans Dome, marked as the blue triangle in Figure 1a) in the GSM during June 2014, a very dry year. In the Southern Appalachian Mountains (SAM), seeder-feeder interactions (SFI) among incoming storm systems and local low-level clouds and fog (LLCF), composed of very high number concentrations of small droplets (< 0.2 mm), lead to enhancement of the surface rainfall intensity up to one order of magnitude at low elevations and in inner mountain valleys (see the map in Figure 1a). Figure 1c demonstrates this effect at a valley station in the inner mountain region during the passage of a frontal system on July 11, 2012, which recorded significantly larger cumulative rainfall in the valley site (P8) compared to the surrounding ridges (P1 and P3). LLCF play a key role in governing plant water budgets, freshwater resources, and the terrestrial energy budget, and tend to be associated with biodiversity hotspots and biogenic aerosol maxima in regions of complex terrain. The ***objective*** of the research presented here is *to elucidate the role of aerosol-cloud interactions in the formation and persistence of LLCF necessary to sustain SFI and high rainfall rates at low elevations*.

A. Cloud Parcel Model

- **Model Features:**
  - **Lagrangian framework**
  - **Hybrid bin structure: moving grid for condensation and stationary grid for coalescence**
- **Major cloud microphysical processes:**
  - **Nucleation**
  - **Condensation**
  - **Collision-coalescence (includes turbulence effects)**
  - **Entrainment (lateral, homogeneous)**
- **Model Outputs:**
  - **Meteorological profiles**
  - **Cloud droplet spectra (e.g., number, volume)**
  - **Derived parameters (e.g., LWC, effective droplet radius, reflectivity)**

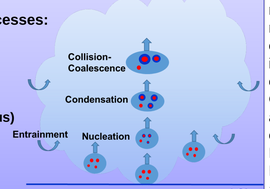

To investigate the influence of aerosol properties (e.g., concentration, size distribution, and hygroscopicity) on LLCF formation, a cloud parcel model was implemented to describe key cloud microphysical processes including nucleation, condensation, collision-coalescence (with turbulence effects included), and lateral homogeneous entrainment (see the schematic at left). Ground-based measurements of aerosol and CCN spectra, and vertical profiles of cloud and rain droplets available from NASA's Integrated Precipitation and Hydrology Experiment (IPHEx) in the SAM are utilized to perform and evaluate modeling studies of fog and feeder-cloud formation.

B. Aerosol-cloud-rainfall Column Model

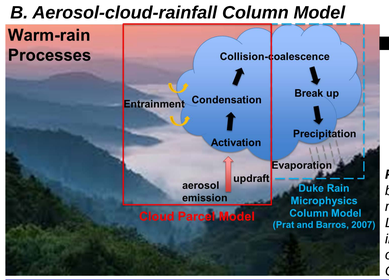

Lidar and Radar Profiling Simulator

Vertical profiles of low-level multi-frequency radar/Lidar signals

Compare with "GPM-proxy" observations from the ER-2 aircraft to identify retrieval errors

Figure 2 – Schematics of the aerosol-cloud-rainfall column model. The blue arrows represent the processes represented by the cloud parcel model (upward) and rain microphysics column model (downward). The Lidar and radar simulator will be coupled to this column model to help interpret IPHEx observations to identify sources of ambiguity in the observations from the satellite-based sensors (e.g., GPM DPR, CALIPSO CALIOP and CloudSat CPR).

GPM mission:

- Compare simulated reflectivity using the aerosol-cloud-rainfall column model with "GPM-proxy" observations from the instrument suite on the ER-2 aircraft
- Characterize errors of GPM core-satellite products to support their retrieval algorithm improvement over complex terrain

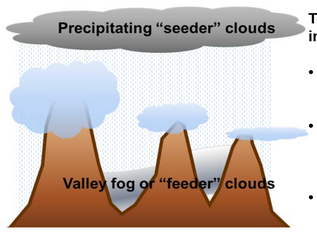

Figure 3 – Conceptual representation of the SFI between precipitating "seeder" clouds and valley fog/ "feeder" clouds over complex terrain.

To probe SFI between LLCF and incoming precipitating systems

- Cloud parcel model: simulate fog/feeder clouds
- Initial top boundary condition of the rain column model: rain drop size distribution (DSD) from MRR
- Rain column model: Raindrops from upper "seeder" clouds interact with small cloud droplets in valley fog/lower "feeder" clouds, resulting in rain enhancement at the surface

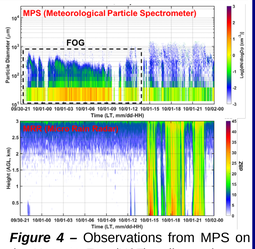

Figure 4 – Observations from MPS on the Haze to Fog (H2F) trailer and a co-located MRR at Elkmont site (see the map in Figure 1a) in 2015.

2. IPHEx Case Study using the Cloud Parcel Model

June 12, 2014

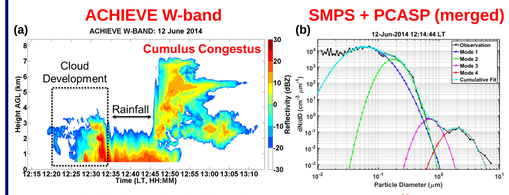

*Figure 2 – a) **Cumulus congestus clouds** observed by the W-band radar at Maggie Valley (MV, see the map in Figure 1a) on June 12, 2014.; b) **Merged surface aerosol particle size distribution** measured by the Scanning Mobility Particle Counter System (SMPS, 1 nm < D< 500 nm) and the Passive Cavity Aerosol Spectrometer (PCASP, 0.1 μm < D< 10 μm) at MV, is fitted by four lognormal distributions. Note aerosol data collected at MV are assumed to represent region aerosol properties.*

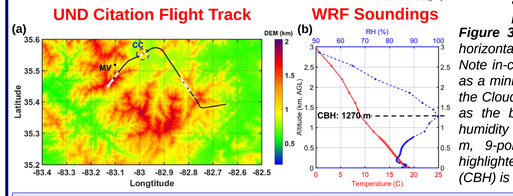

*Figure 3 – a) **UND Citation flight track** during the first horizontal leg (indicated by the black line) on June 12, 2014. Note in-cloud region (indicated by white pluses) is identified as a minimum LWC threshold of 0.25 g/m³, as measured by the Cloud Droplet Probe for updraft velocities. MV is marked as the black asterisk; b) Temperature (red) and relative humidity (blue) **WRF soundings** (horizontal resolution: 250 m, 9-point average) at the core of one cloud (CC), highlighted by the blue circle in a). Note cloud base height (CBH) is 1270 m (indicated by the black dashed line).*

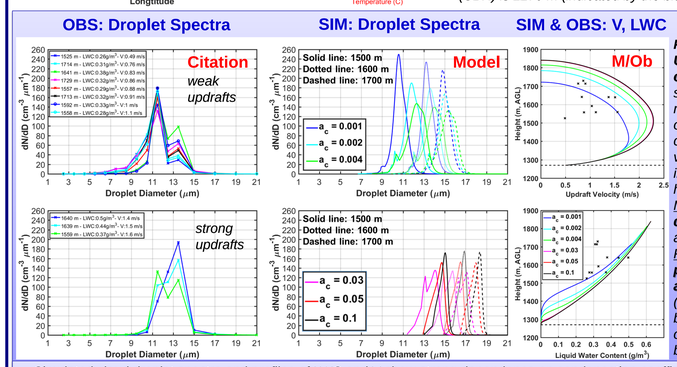

*Figure 7– Left panel: **UND Citation droplet concentration at CC**, sampled at 1-Hz (~ 90m) resolution. Note observed liquid water content (LWC) and vertical velocity (V) are indicated after each height level (AGL); Middle panel: **Simulated droplet concentration** assuming different a_c; Right panel: **Vertical profiles of simulated V and LWC** using different (see color notation in the bottom plot). Citation observations marked as black crosses.*

- Simulated cloud droplet spectra and profiles of LWC and V show strong dependence on condensation coefficient (a_c). Observations support lower values of a_c , likely due to the presence of organic films on natural cloud nuclei which inhibits water uptake.
- Simulated profiles of V and LWC show similar trend with observations. Uncertainties in WRF simulated soundings may partly account for the discrepancies between observed and simulated thermodynamic condition inside the parcel.
- Simulated droplet spectra show good agreement with observations in number concentration and drop size range. Increases in a_c result in a shift towards smaller droplet sizes and lead to broader spectra for small a_c (< 0.01, not shown here) and narrower spectra for large a_c (> 0.01).

3. GPM DPR performance over the SAM

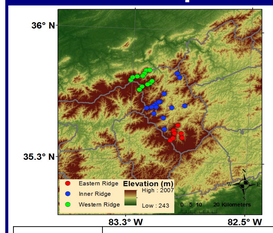

- Near-surface precipitation estimates from GPM-DPR Ka-Band (high sensitivity scans) and Ku-Band (normal scans) were compared with ground observations.
- Time period considered for analysis – March 8, 2014 to May 10, 2016 (Most of the gauges have data till October, 2015).
- Number of Gauges considered for analysis :38 (East: 7; Inner: 16; West: 15).
- Tipping resolution of rain gauges: Eastern Ridge – 0.2 mm/hr, Inner Ridge - 0.1 mm/hr except one gauge (1 mm/hr), Western Ridge – 1.0 mm/hr except 3 gauges (0.1 mm/hr).
- RG that lie within 2.5 km radius of the GPM-DPR pixel were considered for analysis. If more than one RG lie within with 2.5 km radius of GPM-DPR pixel, data from each RG is considered as an independent observations.

Figure 8 – Map of French Broad River Basin showing the long-term rain gauges network.

	Time Window											
	10 min			15 min			30 min			60 min		
	East	Inner	West	East	Inner	West	East	Inner	West	East	Inner	West
Accuracy (Max – 1)	0.978 (0.975)	0.957 (0.974)	0.976 (0.97)	0.975 (0.971)	0.955 (0.971)	0.972 (0.972)	0.968 (0.975)	0.947 (0.964)	0.961 (0.969)	0.952 (0.954)	0.922 (0.939)	0.949 (0.962)
FB (Max – 1)	1 (1.333)	1.083 (1.033)	1.818 (3.75)	0.645 (0.889)	0.963 (0.816)	1.429 (2.143)	0.444 (0.615)	0.672 (0.646)	0.635 (1.11)	0.345 (0.444)	0.422 (0.378)	0.385 (0.5)
POD (Max – 1)	0.55 (0.667)	0.417 (0.533)	0.454 (0.5)	0.484 (0.556)	0.407 (0.474)	0.357 (0.571)	0.422 (0.577)	0.362 (0.396)	0.286 (0.482)	0.328 (0.417)	0.270 (0.268)	0.269 (0.433)
FAR (Max – 0)	0.450 (0.667)	0.667 (0.5)	1.364 (3.25)	0.161 (0.333)	0.556 (0.342)	1.071 (1.571)	0.022 (0.038)	0.310 (0.250)	0.349 (0.63)	0.017 (0.028)	0.151 (0.110)	0.115 (0.067)

Table 1 - Rainfall detection matrix for GPM-DPR Ku Band – NS (Ka-Band – HS) compared to RG observations for different time-scale. Accuracy : (YY + NN) / total; frequency bias: FB = (YY + YN) / (YY + NY); probability of detection: POD = YY /(YY + NY); false alarm ratio: FAR = YN / (YY + Y N). Note: YY -number of hits, NN - correct rejections, YN - false alarms and NY - missed detections.

10- and 30-minute time-window is considered for East and Inner ridge, and West ridge respectively. (This is consistent with TRMM-PR v7 error analysis by Duan et al., 2015).

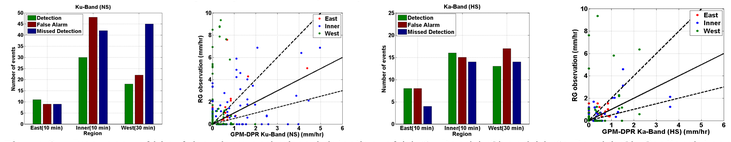

Figure 9 – Frequency of hits, false alarm and missed detection of (a) Ku-Band (NS) and (c) Ka-Band (HS). Scatterplot comparing the RG observations and (b) GPM-DPR Ku-Band (NS) observations and (d) GPM-DPR Ka-Band (HS) observations.

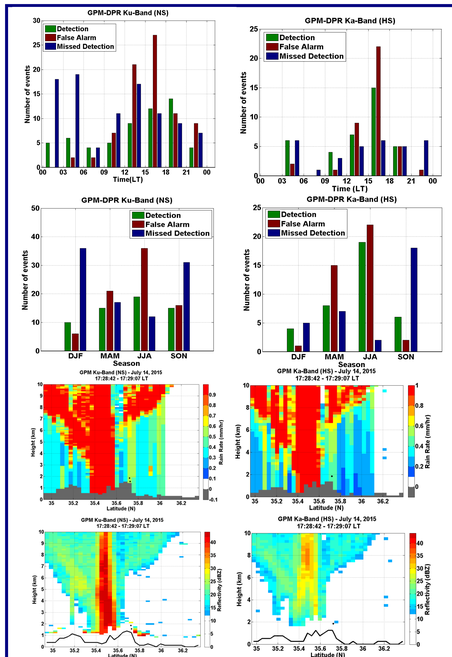

*Figure 10 – **GPM-DPR Error Analysis**: Top Row – **Diurnal Cycle** (a) Ku-Band (NS) and (b) Ka-Band (HS). Bottom Row - **Seasonal Cycle** (c) Ku-Band (NS) and (d) Ku-Band (HS) estimates.*

The number of overpasses is less for HS scans of GPM-DPR Ka-Band because of its narrow swath. The diurnal and seasonal distribution of FA and MD for GPM-DPR Ku-Band NS is consistent with TRMM-PR-v7 distribution from Duan et al., (2015). Mid-day detections remain a problem (9 AM – 3PM LST). MDs overshoot FAs by a factor of 5 between mid-night and early morning (0-6 AM LST. Number of hits is lesser than MD and FA during winter. MDs dominate FAs during Fall and Winter, while FAs dominate MD during Summer. GPM-DPR Ku- and Ka- Band perform similarly.

Light Rainfall (~ 50% of annual totals) remains a challenge in all seasons.

Figure 11 – Top Panel - Rain rate profiles estimated by GPM-DPR Ku- and Ka-Band radar. Bottom Panel - Reflectivity profiles measured by GPM-DPR Ku- and Ka-Band radar. Ku-Band radar overpass over 3 RGs in the western region (2 were collocated) and Ka-Band overpass over 2 collocated RGs. See the pink circle.

GPM-DPR Z-R Error Diagnostics - FAs inconsistent with Measurements

Raingauges (RG300, RG302 and RG402; RG302 and RG402 collocated) **did not observe precipitation.** GPM-DPR estimates: 0.54 mm/hr for Ku-Band NS and 0.47 mm/hr for Ka-band HS.

4. Shallow Precipitation Detection and Classification

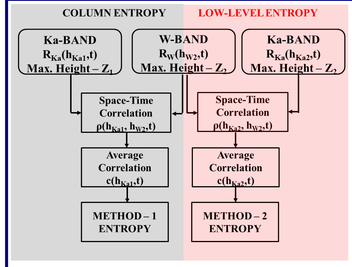

A new **Shallow Rainfall Detection and Classification (SRDC) Algorithm** was developed for collocated W-and Ka-Band ground based radar at Maggie Valley, NC during IPHEx to classify low-level and deep precipitation event. The column and low-level reflectivity profiles of Ka-Band radar and the low-level reflectivity profiles of W-Band are used to compute the column (Method 1) and low-level entropy (Method 2). Method-1 and -2 entropy shows variation for clear sky conditions and precipitation structure. Reflectivity profiles with values less than12 dBZ and 0 dBZ for Ka- and W- Band radar respectively are considered as no-precipitation event. The algorithm was tested on ground-based observations from various locations such as Hyytiala, Finland and Southern Great Plains, Oklahoma.

Figure 12 - Schematic of the SRDC algorithm.

GROUND OBSERVATIONS - IPHEx at Maggie Valley, NC

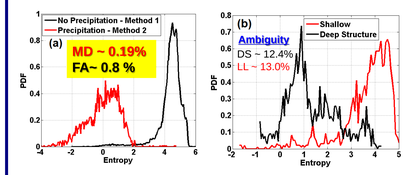

The SRDC algorithm was applied on the collocated W-Band and MRR data at the Maggie Valley, NC during IPHEx-IOP (May 1, 2014 to June 15, 2014). Here, the column profile of W-Band (ACHIEVE) reflectivity is considered to compute Method-1 entropy since the MRR profile is only 1.5 km deep.

Figure 13 - Probability Distribution Function (PDF) of: (a) Rainfall Detection (Method 1 for Non-Rainy Conditions and Method 2 for Rain events) (b) Rainfall Classification into Deep and Low-Level Structure using Method 1 (Column Entropy) and ambiguity error.

SATELLITE OBSERVATIONS : Concurrent GPM-DPR and CloudSat-CPR observations

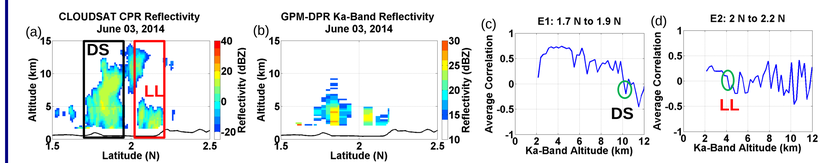

Figure 13 - Reflectivity profiles observed by concurrent overpasses of (a) CloudSar-CPR and (b) GPM-DPR Ka-Band radar from combined 2BCSATDPR product on June 03, 2014 over Kapuas Mountains in Borneo [115 E]. Two distinct events were highlighted – E1 (black box; deep) and E2 (red box). Average of the space-time correlation between column reflectivity profiles of GPM-DPR (till 12 km) and low-level profiles of CloudSat-CPR (till 4 km) for (c) E1 and (d) E2. ***The zero-crossing height of the average correlation curve for the deep and shallow precipitation events is marked by the green circle.***

5. References and Acknowledgements

Arulraj, M., and Barros, A. P., 2016: Shallow Precipitation Detection and Classification using Multifrequency Radar Observations and Model Simulations, IEEE *TGRS*, pending revisions.

Duan, Y., and Barros, A.P., 2016: Mapping Low-Level Clouds and Fog in Complex Terrain: A Climatology Study in the Southern Appalachians Using Satellite Observations and WRF.J. *Geophys. Res. – Atmos.*, submitted.

Duan, Y., Wilson, A. M., and Barros, A. P., 2015: Scoping a field experiment: error diagnostics of TRMM precipitation radar estimates in complex terrain as a basis for IPHEx2014, *Hydrol. Earth Syst. Sci.*, 19, 1501-1520, 10.5194/hess-19-1501-2015.

Prat, O. P., and Barros, A. P., 2007: A Robust Numerical Solution of the Stochastic Collection–Breakup Equation for Warm Rain, *Journal of Applied Meteorology and Climatology*, 46, 1480-1497, 10.1175/jam2544.1.

Wilson, A. M., and Barros, A.P., 2016: Orographic Land-Atmosphere Interactions and the Diurnal Cycle of Low level Clouds and Fog. *J. Hydrometeorology*, pending revisions.

Wilson, A. M., and Barros, A. P., 2015: Landform controls on low level moisture convergence and the diurnal cycle of warm season orographic rainfall in the Southern Appalachians, *Journal of Hydrology*, 531, 475-493, 10.1016/j.jhydrol.2015.10.068.

–**Acknowledgments:** This research is supported by the NASA PMM program.